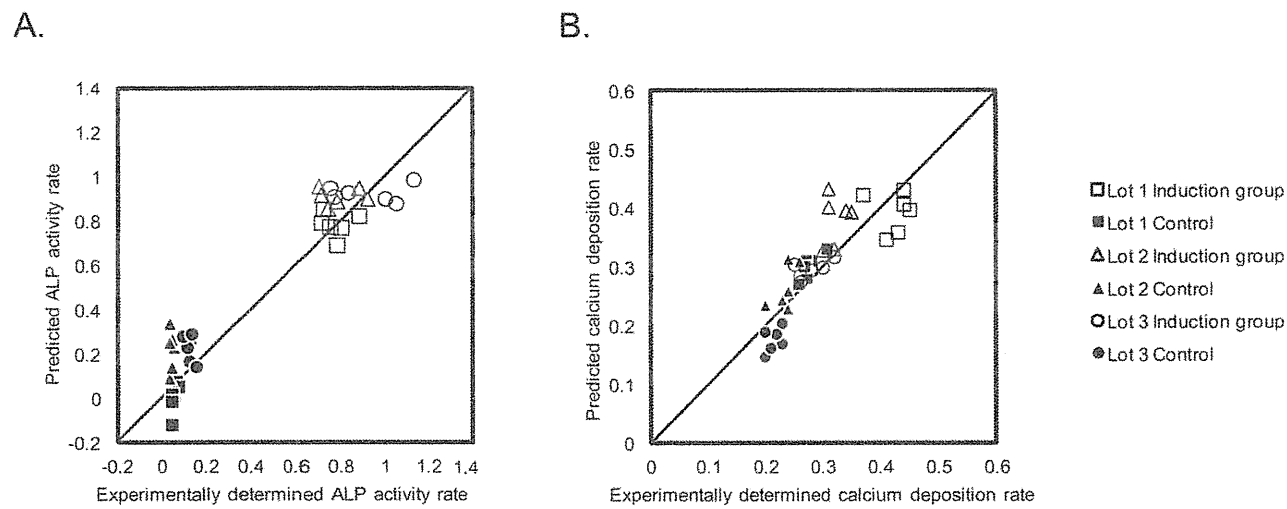

Figure 8. Prediction accuracies in the ongoing patient scheme. A: Scatter plot of experimentally determined values versus predicted values in D14_ALP model, B: Scatter plot of experimentally determined values versus predicted values in D21_Ca model.
doi:10.1371/journal.pone.0055082.g008

Scenario II: Ongoing patient scheme. The ongoing patient prediction scheme is designed to simulate the clinical situation of evaluating a new patient's cell quality with higher accuracy in return for additional data acquisition process (Fig. 5–B). With this scheme, a small sample of the new patient's cells should be differentiated for 14 days as a pilot culture in parallel to the expansion culture. During this pilot culture, cell images are taken to represent the new patient's cellular characteristics. The new patient's data and previous patients' historical data are combined for training the prediction model. Using image data from the next passage and from the 14 day differentiation culture, a prediction can be made prior to the cell harvest (Fig. 5–B). The advantage of this scheme is inclusion of new patient data at the cost of acquiring and inputting new patient images. Characteristics, which may be unique to the new patient, can then be incorporated into training the model with the expectation of a greater predictive value.

The prediction results of the D14_ALP and D21_Ca models are shown in Table 1 and Fig. 8 (see also Fig. 9 and Table S2 for detailed data). These results confirm that the morphological features of hBMSCs observed during differentiation culture highly correlates with the future osteogenic potential. The error ranges were tightened to ± 0.111 with D14_ALP model, and ± 0.037 with D21_Ca model (Fig. 9) as compared to using only historical data to train the model. The standardization of all assay variances to 1.0 results in prediction errors of 0.110 (D14_ALP) and 0.333 (D21_Ca) respectively. Overall, these results suggest that prediction values from Scenario II morphology-based models are nearly 9-fold stable (D14_ALP) or 3-fold stable (D21_Ca) compared to the human assay variances.

When comparing the two scenarios, the prediction accuracies in both prediction models (D14_ALP and D21_Ca) greatly improved in Scenario II, the ongoing patient prediction scheme. These results indicate that incorporation of morphological characteristics from the patient's own cells is extremely important and informative for predicting an individual's BMSC osteogenic potential.

Discussion

Although qualitative cellular morphology is used as a guide for estimating osteogenic differentiation, a quantitative relationship between cellular morphology and biochemical osteogenic markers is not well established. In the present study, we investigated the possibility of predicting osteogenic differentiation of hBMSCs from phase contrast images alone. Specifically, a machine learning algorithm was used to train 14 day cell morphology information and terminal osteogenic biochemical marker values into a model used to predict the terminal marker values from a test set of morphologic data. Our results provide evidence that using this approach can potentially automate and improve decisions, which are currently based on conventional destructive assays and qualitative microscopic assessments.

Using both ALP activity and calcium deposition rates in assessing cellular quality is important to current standard practices. Our proposed modeling schemes allow for accurate prediction of both endpoints. Of particular importance is the accurate prediction of calcium deposition, which is more closely associated with *in vivo* bone formation. For these reasons, constructing different types of prediction models to allow real-time evaluation of the same target cells with multiple aspects and add information for more careful decision making in the culture process. These attributes of an automated computational approach for assessing cellular quality support improvement of safety, efficacy and more rapid and economical scheduling decisions by physicians.

New technology allowing automated image acquisition, which can currently provide more images with greater quality and fewer biases, improves our ability to generate more predictive models based on cellular morphology. In our work, state-of-the art imaging platform (in this study BioStation CT), is the first enhancement technology which lead us to provide uniform and objective data without need for manual optimization of lighting, focusing, or other systematic errors common to manual image acquisition. Operator bias for field selection is also greatly reduced by optimization of the seeding protocol to improve cell distribution together and optimization of the number of fields to view jointly. Image processing biases, the thresholding bias to extract cells from non-cell objects recognized in the images, are also improved by a new automated threshold determination algorithm (data not shown). By preparing three different cell lots and three different passages for cell samples, we aimed to reduce biases of specific patient.

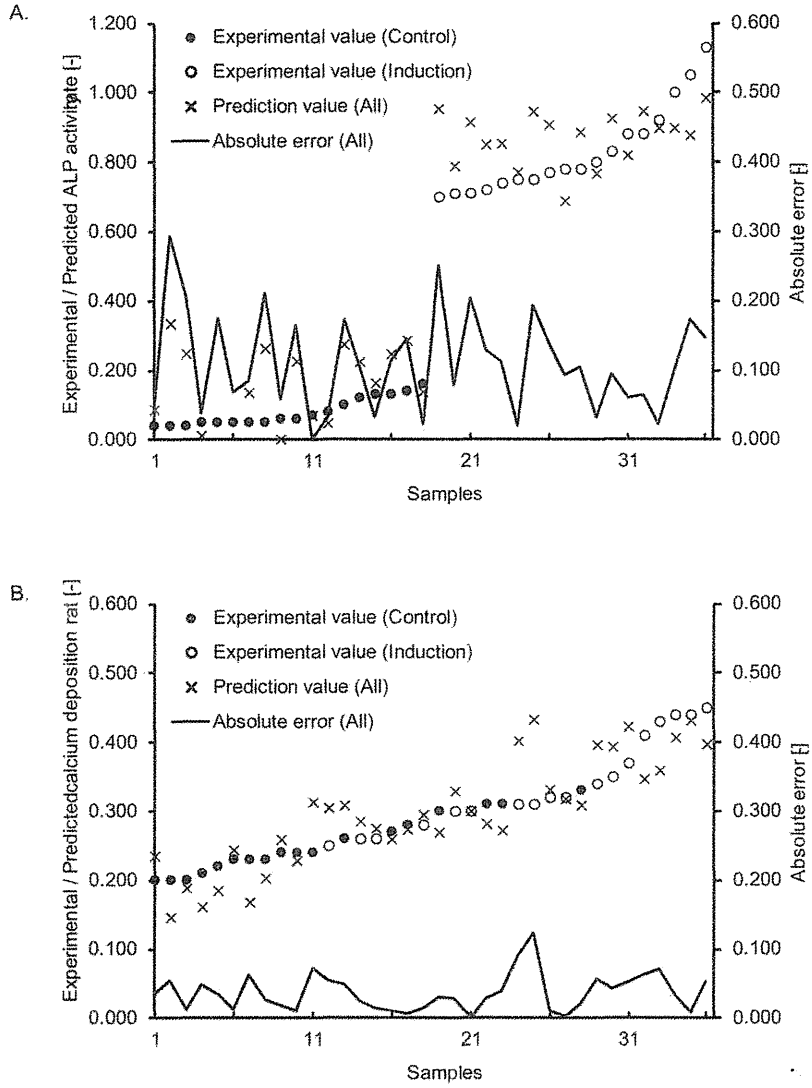

Figure 9. Detailed prediction results in ongoing patient scheme. A: prediction results and error range in the D14_ALP model. B: Prediction results and error range in the D21_Ca model. All the plotted data were rearranged in the order of experimental values.
doi:10.1371/journal.pone.0055082.g009

Table 2. Prediction accuracy of Redge regression models with elimination of each individual features for ALP activity rate.

	New patient prediction scheme		Ongoing patient prediction scheme	
Excluded parameter	**Ave. prediction error* [−]**	**Standardized error** [−]**	**Ave. prediction error* [−]**	**Standardized error** [−]**
Breadth	0.131	0.142	0.078	0.057
Elliptical form factor	0.121	0.124	0.074	0.052
Fiber breadth	0.156	0.197	0.091	0.074
Fiber length	0.136	0.147	0.074	0.051
Hole area	0.141	0.152	0.085	0.060
Inner radius	0.138	0.146	0.088	0.065
Relative hole area	0.134	0.148	0.090	0.065
Shape factor	0.148	0.180	0.108	0.104
Total area	0.136	0.153	0.087	0.064

*Ave. prediction error is the average of the differential between experimentally determined rate and predicted rate.
**Standardized error is calculated by dividing the average of squared errors by variance of all the experimentally evaluated values.
doi:10.1371/journal.pone.0055082.t002

Table 3. Prediction accuracy of Redge regression models with elimination of each individual features for calcium deposition rate.

	New patient prediction scheme		Ongoing patient prediction scheme	
Excluded parameter	**Ave. prediction error* [−]**	**Standardized error** [−]**	**Ave. prediction error* [−]**	**Standardized error** [−]**
Breadth	0.065	0.924	0.028	0.187
Elliptical form factor	0.066	0.972	0.026	0.166
Fiber breadth	0.062	0.870	0.026	0.158
Fiber length	0.065	0.921	0.027	0.164
Hole area	0.065	0.937	0.026	0.138
Inner radius	0.063	0.892	0.028	0.180
Relative hole area	0.060	0.769	0.025	0.146
Shape factor	0.067	0.939	0.029	0.201
Total area	0.067	0.968	0.027	0.160

*Ave. prediction error is the average of the differential between experimentally determined rate and predicted rate.
**Standardized error is calculated by dividing the average of squared errors by variance of all the experimentally evaluated values.
doi:10.1371/journal.pone.0055082.t003

The second enhancement incorporated into this study is the incorporation of robust and continuous morphological features. In this study, it is a key that the morphological features actually used in our modeling are statistical composites (average and standard deviation) of features obtained from all cells from a given condition, which is typically comprised of approximately 4,000–40,000 cells from 15 images for each condition. Such large number of technical replicates offers robustness in each parameter, and effectively enhanced the performance of our prediction model. The continuous image acquisition with precise timing by BioStation CT allowed us to obtain both static morphological features and their dynamic changes throughout the differentiation process. Since morphological changes during osteogenic induction are time-dependent events, it is important to analyze morphological changes with precise timing.

The third enhancement provided by our work stems from the examination of two clinically plausible scenarios. Through these experiments, we found that prediction accuracies of both osteogenic potential measurements greatly increase when the model incorporates training information from early images from the same patient, which reflects individual characteristics in cell morphology. Carefully considering patient-to-patient morphology variation exposes limitations in the current practice of experience-based assessment by culture experts. As indicated in our results, use of new high-content information databases from images, where large amounts of data can be computationally organized and retrieved, is one possible approach for incorporating many aspects related to patient-to-patient variability. Constructing predictive models using historical databases and individualizing new patient predictions by incorporating each new patient's data would be a practical approach to mitigating patient variability while improving the precision of quality assessments.

Comparing the prediction errors of D14_ALP and D21_Ca models in Table 1, the D14_ALP prediction accuracy was higher. One possible explanation for the discrepancy between D14_ALP and D21_Ca predictions is the lack of morphological data during the calcium deposition period, which requires an additional week of culture following two weeks of induction culture. We plan to further investigate ways to enhance predicting this late maturation marker by accumulating more culture images to accrue a larger historical data set. However, we were surprised to discover that without the last seven days of morphology data the D21_Ca model could still predict the final calcium deposition result with reasonable accuracy. To our knowledge, no other reports have been able to accurately estimate the final calcium deposition from early images.

Previous reports have indicated that morphological parameters, similar to the ones used in this study such as flatness or polygonal rate, highly correlate with the osteogenic differentiation potential. Consistent with these reports, we looked at the contribution of each parameter to the prediction performance. In regression analysis, one can examine the effect of each parameter by examining the regression coefficients. Interestingly, among the nine parameters introduced into the regression analysis, there were few sizeable positive or negative coefficients (data not shown). This suggests that there are few dominant morphological parameters that simply correlate to the differentiation potential. Furthermore, when individual features were intentionally eliminated from the model, no significant deterioration was observed in the prediction accuracy (Table 2 and 3). These results suggest that correlation of morphological features and the osteogenic differentiation potential is so complex that there are various compensatory features. Therefore, we conclude that to gain the most robust prediction model for hBMSC osteogenic differentiation potential, all available morphological features throughout the differentiation culture should be incorporated, and biased or feeling-based morphological feature selection should be avoided.

In this work, longitudinal morphological measurements were used as individual, unconnected features, like snapshots. However, to improve the accuracy of the D21_Ca model, we examined ways to incorporate time dependent changes of individual features. With this idea, the same morphological features were converted to change rates between sampling times, analogous to measuring the differences through snapshots. As a result, this morphological feature transformation reduced the D21_Ca model standardized error rate from 0.333 to 0.192 (data not shown). We plan to further investigate the transformation or repeated measurements into time-based trends and patterns in morphological data to improve predictive performance. Our next investigation is designed to further demonstrate applicability and robustness of our proposed method by evaluating the model's ability to characterize "cellular variances", derived from patient diversity, culture protocol effects, and accumulating stresses throughout culture. We also plan to further expand the scope of this work to translate progress made using *in vitro* models and endpoints for morphological prediction of osteogenic potential *in vivo*.

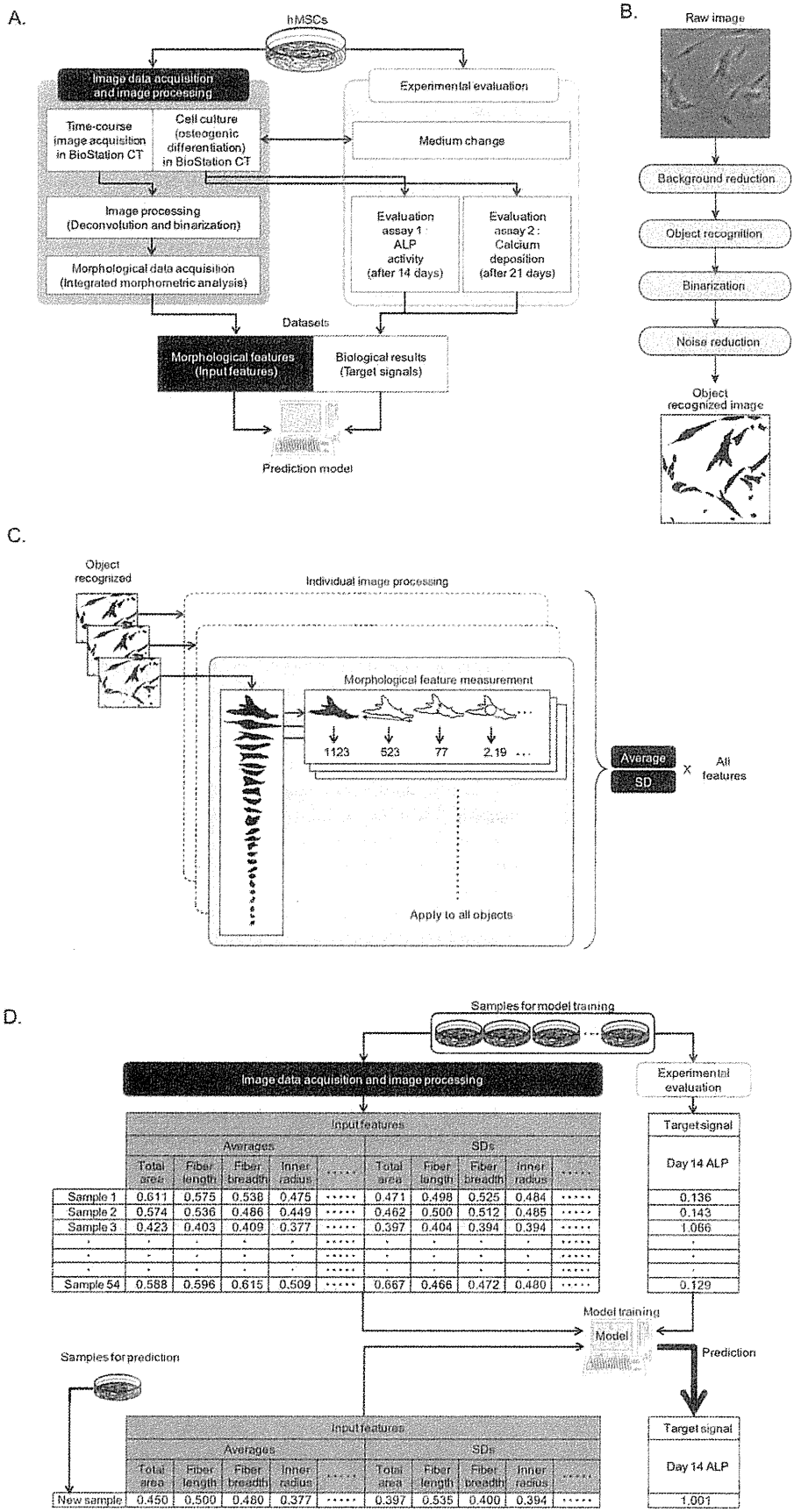

Figure 10. A: Schematic illustration of cell image processing. The raw images were first pre-processed by background reduction processing

by deconvolution and open-close filters. Then, images were binarized by the optimized threshold. The noisy objects were eliminated by particle deletion filter. B: Schematic illustration of cell morphology measurements and data processing. In all object recognized images, all existing objects were measured for the 9 morphological features. Since 1 condition was designed to consist of 3 wells ×5 view fields, all the corresponding object measurement results were processed as a same sample. The average and standard deviation within one sample of all morphological features at each time point were used as the input features for modeling. C: Schematic illustration of prediction model construction. Prediction of differentiation potential consisted of two steps. First, two types of prediction models (D14_ALP model or D21_Ca model) were constructed with the set of image data and experimental evaluation. Second, the values of D14_ALP or the D21_Ca were predicted from the input features of the sample targeted for prediction. The predicted biological rates are compared to the experimentally-determined results to evaluate the accuracy of prediction model.
doi:10.1371/journal.pone.0055082.g010

Materials and Methods

Cells and cell culture

Human bone-marrow derived mesenchymal stem cells (hBMSCs) (Lonza Walkersville, Inc., Maryland, U.S.A.) were subcultured (passaged) in Dulbecco's modified Eagles' medium (DMEM) containing 10% fetal bovine serum (FBS) (Life Technologies Japan Ltd., Tokyo, Japan). Three lots of hBMSCs were designated as Lot 1 (strain number 15000-1, unknown race, Male, 19-year-old), Lot 2 (strain number 17174, Oriental, Male, 20-year-old), and Lot 3 (strain number 11533, Black, Male, 22-year-old), respectively. Lot 1 and 2 were cultured to passages 3, 4, and 5, and Lot 3 was cultured to passages 6, 7, and 8, and cryopreserved for the start of the image acquisition experiment. Cryopreserved cells were seeded at a density of 1.0×10^4 cells/well in 12-well plate (Greiner Bio-One., Frickenhausen, Germany), and the cell-seeding day was designated as day 0 in the image acquisition experiment.

Fig. 1 illustrates the experimental scheme for hBMSC osteogenic differentiation culture. From day 0 to 3, cells were cultured in 10% FBS-containing α-modified Eagle's medium (αMEM) (Sigma-Aldrich Co., St. Louis, MO, U.S.A.). From day 4 to 18, cells were divided into two groups: (1) Osteogenic induction group (Induction, N = 6) and (2) Non-induction group (Control, N = 6). For the induction group, the medium was switched to induction medium consisting of 10% FBS-containing αMEM medium supplemented with 10 nM dexamethasone (Sigma-Aldrich Co.), 100 mM ascorbic acid (Wako Pure Chemical Industries, Ltd., Osaka, Japan), and 10 mM glycerol 2-phosphate sodium salt hydrate (Sigma-Aldrich Co.). For the non-induction group, supplements were not added to the 10% FBS-containing αMEM medium. The appropriate medium was changed at day 7 and day 13. For half of the samples in each experimental group (n = 3), alkaline phosphatase (ALP) activity were quantified on day 18. The remaining samples continued culture until day 25, and calcium deposition was quantified on day 25.

Image acquisition

Figs. 1 and 10-A illustrates the image acquisition scheme during hBMSC osteogenic differentiation culture. From day 0 to day 13 (14 days), phase contrast microscopic images of hBMSCs were obtained using the BioStation CT (Nikon Corporation, Tokyo, Japan). BioStation CT is an automatic cell maintenance system, which maintains a stable incubation environment (37°C, 5% CO_2, 100% humidity) with scheduled automatic image acquisition. The number of view fields was optimized to five, which provides the least error for estimating the correct cell seeding for each well. Five view fields (center position and four positions 2.2 mm from the center) of phase contrast images were acquired from each well with fully automatic focusing. The phase contrast images had the least noise and background when using the halo-reduction lens. Image acquisition timing was set to every 8 hours from day 4 to 18 (magnification = 10x). Time points are designated as time 0 to 38, indicating each of the 8 hour imaging intervals. Data at time 0 was omitted, since the cells were not fully settled. Data at time 7 and time 26 were also omitted, since it was concurrent with medium changes for each well plate, resulting in 36 time-points as a total.

Quantification of ALP activity

Quantitative ALP activity assays were performed as previously described [9]. After 18 days of culture, cell number was measured using a cell counting kit-8 (WST-8®; Dojindo Laboratories, Kumamoto, Japan), and ALP activities were measured with a p-nitrophenyl phosphate solution (Lab Assay ALP®; Wako Pure Chemical Industries, Ltd.). Briefly, for cell count, 100 µl of WST-8 was added to each well containing 1 mL of fresh medium, incubated for 1 hour, and absorbance was read at 450 nm. After WST-8 analysis, each well was washed twice with phosphate buffered saline (PBS) and 800 µL of p-nitrophenyl phosphate solution was added to each well. After 10 min of incubation at 37°C, the conversion to p-nitrophenol was stopped with 800 µl of 3N NaOH and the absorbance of p-nitrophenol was measured at 405 nm. Alkaline phosphatase-specific activity is expressed as p-nitrophenol absorbance (OD; 405 nm)/WST-8 absorbance (OD; 450 nm).

Calcium deposition quantification

After 25 days of culture, cells were fixed with 70% ethanol for 1 hour, washed, and stained for 10 min with 40 mM alizarin red S solution (pH: 4.2). After washing with PBS, plates were incubated with 10% cethylphridinium chloride for 15 min. Thereafter, supernatants were collected from each well and the absorption of each supernatant was measured at 405 nm to determine the amount of calcium deposition.

Cell image processing

All images (.bmp files) were processed by MetaMorph (Molecular device, CA, U.S.A) with the original combination of image-processing filter sets (Fig. 10–A). Briefly, the raw images were pre-processed by open-close filters and binarized by the optimized threshold. All image data was pre-processed using the same brightness threshold, which was optimized by 20 randomly picked image samples. This pre-processing step minimized error between the manually determined image cell number and the number of objects determined after pre-processing. After binarization, all individual objects in each image, consisting of cells and noise (non-cell objects), were measured by the integrated morphometric analysis function to measure morphological features (9 morphological features are: Breadth, Elliptical form factor, Fiber breadth, Fiber length, Hole area, Inner radius, Relative hole area, Shape factor, Total) (Fig. 10–B). The morphological features were carefully selected with the MetaMorph measurement function by logical selection. Features related to color and brightness were excluded first. Second, independent features were selected by hierarchical clustering and highly correlated features ($R>0.85$) were excluded. From the data consisting of object ID and its standardized 9 morphological features (average = 0, standard deviation = 1), the noise data (non-cell objects) was automatically cleansed by the original noise-reduction algorithm

prior to the analysis (patent pending). From the pre-processed data, average (AVE) and standard deviation (SD) from each of the 9 morphological features was calculated from each of the cell objects covering five view fields from the same well, and used as the 18 inputs (9 features with AVE and SD) for each sample to be used in further analysis (Fig. 10–C). The morphological features and cell number (AVE and SD for 19th and 20th feature) from each well were then tagged with the target signals, which are experimentally determined values, resulting in 54 samples (= 3 lots ×2 induction conditions ×3 passages ×3 wells) tagged with ALP values, and 54 samples tagged with calcium deposition values. This process links the "result" (biological measurement) with the "indication" (image-derived morphological feature), to derive a dataset for further modeling (Fig. 10–D).

Construction and evaluation of prediction model

Prediction of differentiation potential consists of two steps (Fig. 10–D): one is the construction of a prediction model, and the other is the evaluation of the constructed model. Using Ridge regression, two types of prediction models were constructed: (1) D14_ALP model, and (2) D21_Ca model. For the new patient scheme, prediction models were trained with 36 samples from 2 lots, and 18 samples from the remaining single lot were predicted. For the ongoing patient scheme, prediction models were trained with 42 samples from 2 lots of 3 passages plus the samples from new lot of 1 or 2 passages were used for training, and 12 samples from the remaining 1 lot were predicted (Fig. 5). The detailed modeling process is described in a previous report (See Section 3 in [18] for details of the Ridge regression method). The performance of each of the models and datasets were evaluated by the average accuracy resulting from leave-one-out cross validation.

For the evaluation of our proposed scheme, two evaluation indices are introduced in our work. One index is the correlation coefficient (R) of actual assay values and prediction values, which evaluates the prediction accuracy and its data coverage. The higher R increases, the more the model is capable of predicting "differentiation marker values" with small error rate. The other index of evaluation that we introduced is the average of absolute error. This value is calculated by obtaining absolute values of (experimentally determined value minus the predicted value). To compare these errors, we standardized these errors by dividing the variance of total experimentally determined values in one assay.

Supporting Information

Table S1 * Exp. determined rate is the abbreviation of the experimentally determined rate.
(XLS)

Table S2 * Exp. determined rate is the abbreviation of the experimentally determined rate.
(XLSX)

Acknowledgments

We are grateful to Mai Okada and Yurika Nonogaki for supporting the experiments and data storage. We also thank Wakana Yamamoto, Yoshihide Nagura, Kazuhiro Mukaiyama, Kenji Kojima, Hiroto Sasaki, and Asuka Miwa for establishing basal analysis protocol and algorithms for image analysis procedure.

Author Contributions

Conceived and designed the experiments: FM HK HA RK. Performed the experiments: FM. Analyzed the data: IT FM RK. Contributed reagents/materials/analysis tools: HS YK HH RK. Wrote the paper: FM IT HK HA RK.

References

1. Wu Y, Chen L, Scott PG, Tredget EE (2007) Mesenchymal stem cells enhance wound healing through differentiation and angiogenesis. Stem Cells 25: 2648–2659.
2. Chen L, Tredget EE, Wu PY, Wu Y (2008) Paracrine factors of mesenchymal stem cells recruit macrophages and endothelial lineage cells and enhance wound healing. PLoS ONE 3: e1886.
3. Barry FP, Murphy JM (2004) Mesenchymal stem cells: clinical applications and biological characterization. Int J Biochem Cell Biol 36: 568–584.
4. Hayashi O, Katsube Y, Hirose M, Ohgushi H, Ito H (2008) Comparison of osteogenic ability of rat mesenchymal stem cells from bone marrow, periosteum, and adipose tissue. Calcif Tissue Int 82: 238–247.
5. Mizuno D, Kagami H, Mizuno H, Mase J, Usami K, et al. (2008) Bone regeneration of dental implant dehiscence defects using a cultured periosteum membrane. Clin Oral Implants Res 19: 289–294.
6. Olivo C, Alblas J, Verweij V, van Zonneveld AJ, Dhert WJ, et al. (2008) In vivo bioluminescence imaging study to monitor ectopic bone formation by luciferase gene marked mesenchymal stem cells. J Orthop Res 26: 901–909.
7. Kagami H, Agata H, Tojo A (2011) Bone marrow stromal cells (bone marrow-derived multipotent mesenchymal stromal cells) for bone tissue engineering: Basic science to clinical translation. Int J Biochem Cell Biol. 43: 286–289.
8. Dennis JE, Esterly K, Awadallah A, Parrish CR, Poynter GM, et al. (2007) Clinical-scale expansion of a mixed population of bone-marrow-derived stem and progenitor cells for potential use in bone-tissue regeneration. Stem Cells 25: 2575–2582.
9. Agata H, Asahina I, Yamazaki Y, Uchida M, Shinohara Y, et al. (2007) Effective bone engineering with periosteum-derived cells. J Dent Res 86: 79–83.
10. Platt MO, Wilder CL, Wells A, Griffith LG, Lauffenburger DA. (2009) Multipathway kinase signatures of multipotent stromal cells are predictive for osteogenic differentiation: tissue-specific stem cells. Stem Cells. 27:2804–2814.
11. Kelly DJ, Jacobs CR (2010) The role of mechanical signals in regulating chondrogenesis and osteogenesis of mesenchymal stem cells. Birth Defects Res C Embryo Today. 90:75–85.
12. Kino-Oka M, Maeda Y, Sato Y, Maruyama N, Takezawa Y, et al. (2009) Morphological evaluation of chondrogenic potency in passaged cell populations. J Biosci Bioeng.107:544–551.
13. Carpenter AE, Jones TR, Lamprecht MR, Clarke C, Kang IH, et al. (2006) CellProfiler: image analysis software for identifying and quantifying cell phenotypes. Genome Biol. 7: R100.
14. Misselwitz B, Strittmatter G, Periaswamy B, Schlumberger MC, Rout S, et al. (2010) Enhanced CellClassifier: a multi-class classification tool for microscopy images. BMC Bioinformatics. 11: 30.
15. Harder N, Mora-Bermudez F, Godinez WJ, Wunsche A, Eils R, et al. (2009) Automatic analysis of dividing cells in live cell movies to detect mitotic delays and correlate phenotypes in time. Genome Res. 19: 2113–2124.
16. Jones TR, Carpenter AE, Lamprecht MR, Moffat J, Silver SJ, et al. (2009) Scoring diverse cellular morphologies in image-based screens with iterative feedback and machine learning. Proc. Natl. Acad. Sci. U. S. A. 106: 1826–1831.
17. Hoerl AE and Kennard R (1970) Ridge regression: biased estimation for nonorthogonal problems. Technometrics 12: 55–67.
18. Hastie T (2009) The Elements of Statistical Learning: Data Mining, Inference, and Prediction. Springer-Verlag. 43.

blood

2013 122: 4259-4263
doi:10.1182/blood-2012-08-451278 originally published online October 30, 2013

In vivo leukemogenic potential of an interleukin 7 receptor α chain mutant in hematopoietic stem and progenitor cells

Kazuaki Yokoyama, Nozomi Yokoyama, Kiyoko Izawa, Ai Kotani, Akira Harashima, Katsuto Hozumi and Arinobu Tojo

Blood (print ISSN 0006-4971, online ISSN 1528-0020), is published weekly by the American Society of Hematology, 2021 L St, NW, Suite 900, Washington DC 20036.

Brief Report

LYMPHOID NEOPLASIA

In vivo leukemogenic potential of an interleukin 7 receptor α chain mutant in hematopoietic stem and progenitor cells

Kazuaki Yokoyama,[1,2] Nozomi Yokoyama,[3] Kiyoko Izawa,[1] Ai Kotani,[4] Akira Harashima,[5] Katsuto Hozumi,[2] and Arinobu Tojo[1]

[1]Division of Molecular Therapy, Advanced Clinical Research Center, Institute of Medical Science, University of Tokyo, Tokyo, Japan; [3]Department of Laboratory Medicine, Research Hospital, Institute of Medical Science, University of Tokyo, Tokyo, Japan; [2]Department of Immunology and [4]Institute of Innovation Science and Technology, Tokai University School of Medicine, Kanagawa, Japan; and [5]Cell Biology Institute, Research Center, Hayashibara Biochemical Laboratories, Okayama, Japan

Key Points

- Gain-of function mutation of IL7Rα induces lymphoid leukemia as well as myeloproliferative disease.
- In vivo oncogenicity of mutant IL7Rα is influenced by the differentiation stage at which it occurs.

Somatic gain-of-function mutations in interleukin 7 receptor α chain (IL7Rα) have been described in pediatric T and B acute lymphoblastic leukemias (T/B-ALLs). Most of these mutations are in-frame insertions in the extracellular juxtamembrane-transmembrane region. By using a similar mutant, a heterozygous in-frame transmembrane insertional mutation (INS), we validated leukemogenic potential in murine hematopoietic stem/progenitor cells, using a syngeneic transplantation model. We found that ectopic expression of INS alone in hematopoietic stem/progenitor cells caused myeloproliferative disorders, whereas expression of INS in combination with a Notch1 mutant led to the development of much more aggressive T-ALL than with wild-type IL7Rα. Furthermore, forced expression of INS in common lymphoid progenitors led to the development of mature B-cell ALL/lymphoma. These results demonstrated that INS has significant in vivo leukemogenic activity and that the lineage of the resulting leukemia depends on the developmental stage in which INS occurs, and/or concurrent mutations. (*Blood*. 2013;122(26):4259-4263)

Introduction

Interleukin 7 (IL7) is essential for T-cell development and homeostasis.[1] Its cognate receptor (IL7R) forms a heterodimer composed of the α chain (IL7Rα) and common γ chain; binding of IL7 to IL7R triggers activation of Janus kinase (JAK)/signal transducer and activator of transcription signaling and the PI3K/v-akt murine thymoma viral oncogene homolog 1 (Akt) pathways.[1]

Accumulating evidence has demonstrated that dysregulation of the IL7 signaling axis may be implicated in lymphoid malignancies. For example, IL7 transgenic mice develop T- and B-cell lymphomas,[1] and human primary T-cell acute lymphoblastic leukemia (T-ALL) cells respond to IL7 in vitro[1] and in vivo.[2] Moreover, recent findings describing IL7Rα gain-of-function mutations in pediatric ALL and a T-ALL cell line have provided direct evidence that the IL7-IL7R axis plays a crucial role in the pathogenesis of human ALL.[3-6]

Although the gain-of-function properties of these mutants have been precisely studied in vitro,[3-5] their leukemogenic potential in vivo has not been well studied. One study reported that T-cell leukemogenesis was triggered by an IL7Rα mutant.[5] However, they used murine IL7-dependent D1 progenitor T-cell lines derived from p53-knockout mice,[7] which spontaneously develop T-cell lymphoma,[8,9] and this specific animal model may not be generally applicable.

To extend these observations, we demonstrate the in vivo leukemogenic potential of such a mutant when expressed in primary hematopoietic stem and progenitor cells by using a IL7Rα mutant, which was previously identified in a T-ALL cell line.[6]

Methods

Mice

Six- to 12-week-old Balb/c mice were used for all experiments. Lineage depletion of bone marrow (BM) or embryonic day 14.5 (E14.5) fetal liver was performed by the EasySep Mouse Hematopoietic/Progenitor Cell Enrichment Kit (StemCell Technologies). Via tail vein injection, 1×10^6 Lineage$^-$ BM/fetal liver cells (lin$^-$ cells), pro-B, or Thy1$^+$T cell progenitors were injected into lethally (8 Gy) or sublethally (4 Gy) irradiated recipients. Mice were maintained in accordance with institutional animal care guidelines (Institute of Medical Science, University of Tokyo). Detailed methods are provided in the supplemental Methods.

Submitted August 20, 2012; accepted October 10, 2013. Prepublished online as *Blood* First Edition paper, October 30, 2013; DOI 10.1182/blood-2012-08-451278.

K.Y. and N.Y. contributed equally to this study.

The online version of this article contains a data supplement.

There is an Inside *Blood* commentary on this article in this issue.

The publication costs of this article were defrayed in part by page charge payment. Therefore, and solely to indicate this fact, this article is hereby marked "advertisement" in accordance with 18 USC section 1734.

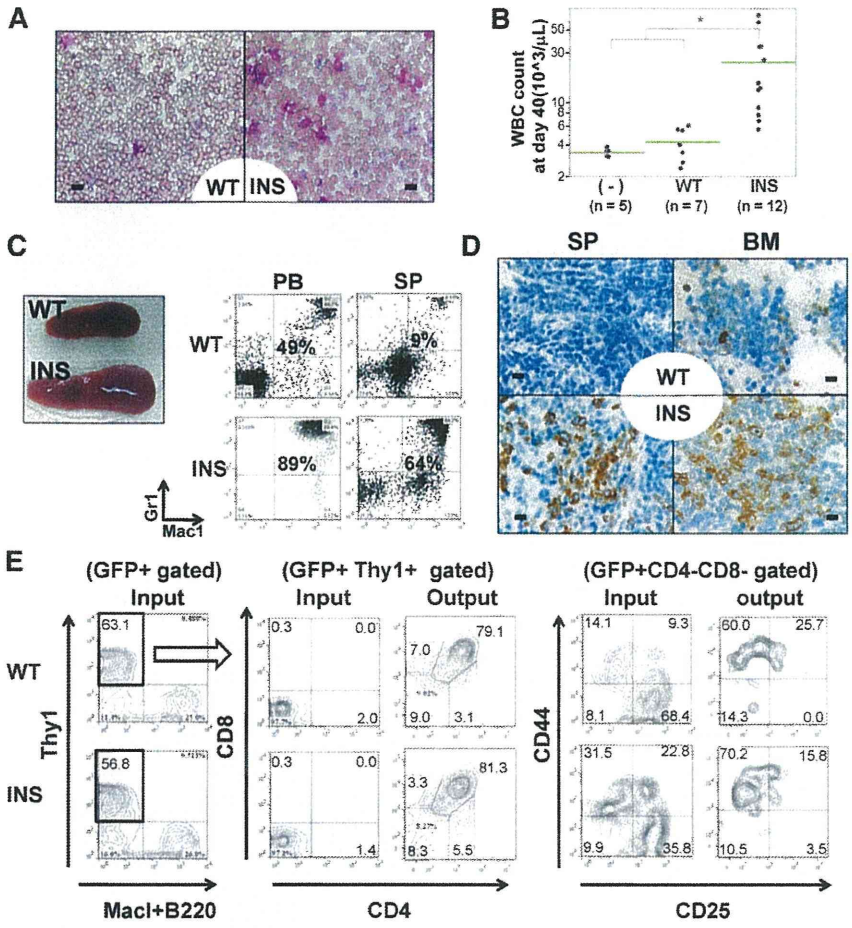

Figure 1. In vivo transforming activity of INS. (A-D) Lin$^-$ cells were retrovirally transduced with mock vectors (mock), WT, or INS, followed by injection into lethally irradiated congenic mice. (A) May-Giemsa staining of PB smears at day 40, showing marked leukocytosis consisting predominantly of mature myeloid cells. (B) White blood cell count at day 40. *$P < .05$ (analysis of variance; INS vs WT or mock recipient mice). (C) FACS of the PB and SP at day 40, showing an increase in Mac-1$^+$/Gr-1$^+$ myeloid cells. (D) Immunohistochemical analysis (IHC) of SP and BM specimens by anti-myeloperoxidase, indicating an increase in the number of myeloid cells in INS recipient mice. Bars represent (A) 10 μm and (D) 20 μm. (E) Demonstration of in vivo reconstitutive capacity of hIL7R (WT/INS) transduced T-cell progenitors. Lin$^-$ kit$^+$ stem/progenitor cells were cultured on OP9-DL1 stromal layer for 7days, supplemented with mIL7$^+$ human Fms-like tyrosine kinase 3-ligand, which allowed them to differentiate into Thy1$^+$CD25$^-$CD44$^+$DN1 immature T-cell progenitor fractions. These cells were retrovirally transduced with WT/INS vector. The resultant cells were allowed to expand on OP9-DL1 stroma for additional 7 to 10 days, and developed into CD25$^+$CD44$^-$ DN3 immature T-cell progenitor fractions. These Thy1$^+$ cells were green fluorescent protein (GFP)-sorted and intravenously injected into sublethally irradiated mice. The resultant GFP$^+$ thymic seeding progenitors (denoted as "input") in recipient mice of WT and INS at day 52 was shown (denoted as "output").

Results and discussion

In vitro transforming activity of the mutant IL7Rα, INS

Consistent with previous report, sequencing analysis of exon 6 of the IL7Rα gene, mainly encoding the transmembrane domain, identified a heterozygous in-frame transmembrane insertional mutation (INS) in the T-ALL cell line DND-41.[6] Forced expression of INS exerted transforming activity in Ba/F3 cells, as revealed by acquisition of cytokine-independent growth (supplemental Figure 1A-C, found on the *Blood* website) as well as the autonomous phosphorylation of Stat1, Stat3, Stat5, and Akt (supplemental Figure 1D). In addition, transient expression of IL7Rα in human embryonic kidney 293 cells leads to autonomous tyrosine phosphorylation of Jak1 only in those expressing INS (supplemental Figure 1D, *left*), suggesting that INS constitutively activated IL7R downstream signals via Jak1. As INS falls within the same category of reported mutation of IL7Rα,[3-6] we decided to use INS as a representative gain-of-function IL7Rα mutation for further experiments.

INS in stem/progenitor cells caused myeloproliferative disorders

The leukemogenic activity of INS and wild-type (WT) IL7Rα was assessed by retroviral transduction of Lin$^-$ cels. Within 6 to 9 weeks after transplantation, recipient mice transplanted with INS Lin$^-$ cells, but not WT Lin$^-$ cells, developed myeloproliferative disorders (MPDs) characterized by splenomegaly, leukocytosis, and polycythemia (Figure 1A-C, *right*; supplemental Figures 1D and 3C-D). Fluorescence-activated cell sorter (FACS) and morphological analysis revealed a marked increase in Mac1^{++} Gr-1^{++} mature myeloid cells in the peripheral blood (PB), spleen (SP), and BM (Figure 1C-D; supplemental Figures 2 and 4). An increase of Ter119$^+$ CD71$^+$ immature erythroblast was also noted in SP and BM (supplemental Figure 4, SP; data not shown). INS-induced MPD was oligoclonal, as evidenced by Southern blot analysis (supplemental Figure 5, *left*). A similar disease phenotype was also observed in mice transplanted with Lin$^-$c-Kit^{++}Sca1^{++} (KSL) fractions transduced with INS (supplemental Figures 3A-B,E and 4). Both B- and T-cell development were severely perturbed in INS recipient mice (supplemental Figure 4). As transplantation of INS-transduced KSL cells resulted in preferential expansion of myeloid progenitor–enriched Lin$^-$c-Kit^{++}Sca1$^-$ fraction (supplemental Figure 6), we speculate that in vitro transforming activity of INS skewed myeloid progenitor expansion at the expense of common lymphoid progenitor Lin–c-kit^{low}Sca1$^+$ IL7Rα$^+$ (CLP) expansion, through which normal lymphopoiesis might be perturbed. This was also supported by the fact that INS exerted transforming activity in input KSL cells, as well as resultant myeloid progenitors ex vivo, as revealed by colony-forming cell assay (supplemental Figure 7). It was previously reported that forced expression of wild-type murine IL7Rα into IL7Rα knockout BM progenitors induces a very similar MPD phenotype, including

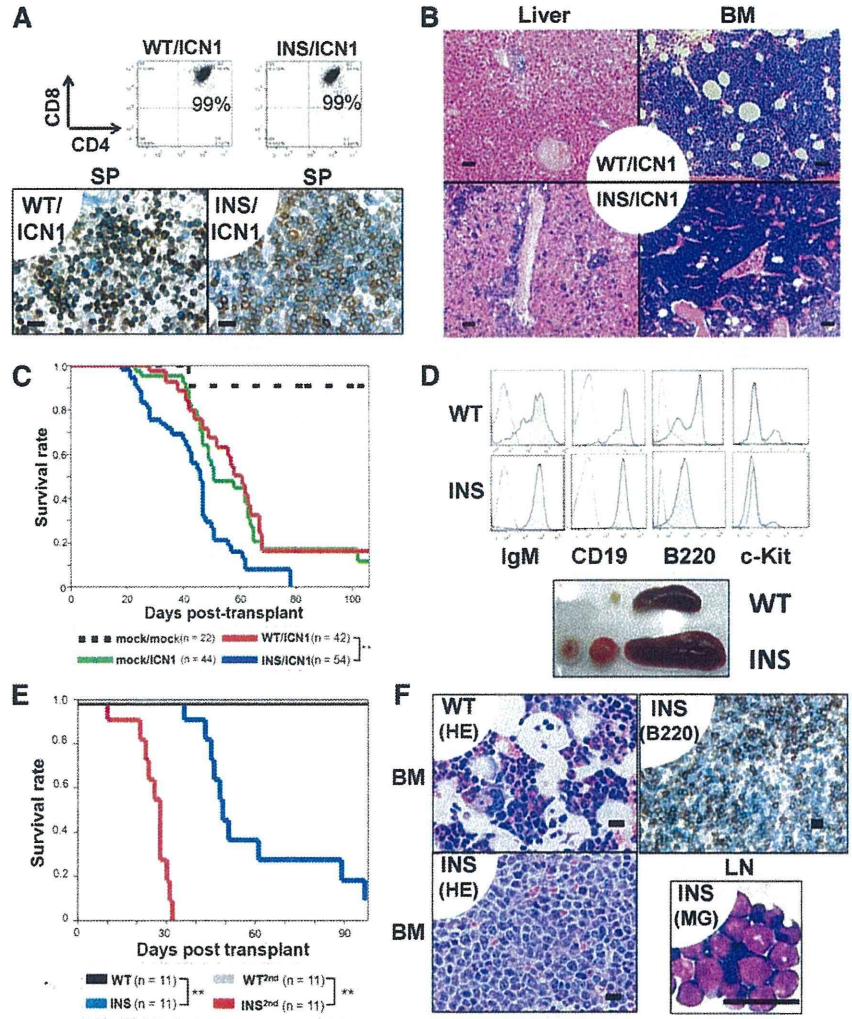

Figure 2. INS synergized with active Notch1 (A-C) and exerted transforming activity in CLPs (D-F) in vivo. (A-C) Lin$^-$ cells were cotransfected with vectors encoding the ICN1 gene (mock, ICN1) and the hIL7R gene (mock, WT, INS), followed by injection into lethally irradiated congenic mice. (A, *upper*) FACS analysis of the SP from WT/ICN1 or INS/ICN1 recipient mice at day 40. Data were obtained from GFP$^+$ (marker for the ICN1 gene) and rat CD2$^+$ (marker for the hIL7R gene) fractions. (A, *lower*) IHC of SP specimens using anti-CD3 antibodies from WT/ICN1 (*left*) and INS/ICN1 (*right*) recipient mice. Bar represents 20 μm. (B) Histological findings of liver (*left 2 panels*) and BM (*right 2 panels*) from WT/ICN1 (*upper*) and INS/ICN1 (*lower*) recipient mice (hematoxylin and eosin stain). Bar represents 50 μm. (C) Survival curves of recipient mice (mock/mock, n = 22; mock/ICN1, n = 44; WT/ICN1, n = 42; INS/ICN1, n = 54) $^{**}P < .01$ (log-rank test). (D-F) CLPs transfected with hIL7R constructs were expanded in vitro for 18 days and injected into sublethally irradiated congenic mice. (D, *top 2 panels*) FACS analysis of the BM: WT recipient mice at day 60 (WT) and INS recipient mice at day 60 (INS). Data are obtained from GFP$^+$ gated fractions. Open histogram, isotype control; shaded histogram, specific staining. (D, *lower*) Splenomegaly and lymphadenopathy developed in CLPs-INS recipient mice at day 60 (denoted as "INS"). (E) Survival curves of recipient mice (n = 11 for each condition). $^{**}P < .01$ (log-rank test, INS vs WT or INS vs INS^{2nd}). (F) Histological findings: BM specimens from WT recipient mice (*upper left*) and INS recipient mice at day 60 by hematoxylin and eosin stain (*lower left*) or by IHC of B220$^+$ cells (*upper right*). Lymph node cytospin from INS recipient mice at day 60 by May-Giemsa stain (*lower right*). Bar represents 20 μm. WT, WT primary recipients; INS, INS primary recipients; WT-2nd, WT day 30 BM secondary recipients; INS-2nd, INS day 30 BM secondary recipients.

splenomegaly resulting from neutrophilia.[10] Consistent with this report, transduced WT appeared to induce some degree of increase in myeloid fraction and neutrophilia in PB and SP compared with that of mock increase of myeloid fraction and neutrophilia in PB (supplemental Figure 4). Importantly, the magnitude was quite different, as we could not find a statistically significant difference of SP weight in mock and WT (n = 4 each; $P = .61$, 1-way analysis of variance; supplemental Figure 3C). This is in contrast to the difference of INS (n = 4) and WT ($P < .01$; supplemental Figure 3C). WT-induced mild myeloid expansion was accompanied by concomitant increase in lymphoid subset in PB, SP, and BM, specifically CD19$^+$ B-cell fractions (supplemental Figure 4). Considering the fact that the phenotype of WT-recipient mice was different from that of mock (supplemental Figure 4), it should be mentioned that we could not rule out the possibility that the phenotype elicited by INS is in part a result of the effect of IL7R overexpression per se, irrespective of its mutational status. The major difference from the previous report was that they rescued the loss-of-function phenotype of IL7Rα by ectopic expression of IL7Rα.[10]

Neither of these recipient mice developed overt leukemia throughout the median follow-up period of 5 months (WT, n = 28; INS, n = 22), suggesting that additional transforming events are required for clonal evolution to aggressive leukemia. Considering the fact that recipient mice for hematopoietic stem cells transduced with constitutively active Akt or signal transducer and activator of transcription-5 also developed similar diseases together,[11,12] this MPD phenotype is likely to be induced by stem cells ectopically expressing INS.

Nononcogenic consequence of INS in T-cell progenitors

Next, we wished to test the effect of INS on T-cell precursors. Toward this aim, we cocultured Lin$^-$ kit$^+$ stem/progenitor cells for 7 days, which allowed the emergence of Thy1$^+$CD25$^-$CD44$^+$DN1 immature T-cell-progenitor fractions (data not shown). These cells were transduced by retroviral transduction of the WT/INS vector. The resultant transduced cells were allowed to expand on OP9 expressing the Notch ligand Delta-like 1 (OP9-DL1) stroma for an additional 7 to 10 days, which allowed them to develop Thy1$^+$ CD4$^-$CD8$^-$CD25$^-$CD44$^+$DN1 to DN3 CD25$^+$CD44$^-$DN3 immature T-cell-progenitor fractions (Figure 1E). The resultant Thy1$^+$ cells were GFP sorted and injected into sublethally irradiated mice. As a result, we could detect stable engraftment of GFP$^+$ T-cell progenitors in recipient mice from day 40 to day 50 in thymus (Figure 1E) and CD4 or CD8 single-positive cells in the periphery, such as SP or PB (data not shown). Neither of these recipient mice